Mon. Not. R. Astron. Soc. **000**, 000–000 (0000) Printed 4 October 2010 (MN LATEX style file v2.2)

Cosmography with cluster strong lenses: the influence of substructure and line-of-sight halos

Anson D'Aloisio[1⋆] & Priyamvada Natarajan[1,2]†
[1]*Department of Physics, Yale University, PO Box 208120, New Haven, CT 06520-8120*
[2]*Department of Astronomy, Yale University, PO Box 208101, New Haven, CT 06511*

4 October 2010

ABSTRACT
We explore the use of strong lensing by galaxy clusters to constrain the dark energy equation of state and its possible time variation. The cores of massive clusters often contain several multiply imaged systems of background galaxies at different redshifts. The locations of lensed images can be used to constrain cosmological parameters due to their dependence on the ratio of angular diameter distances. We employ Monte-Carlo simulations of cluster lenses, including the contribution from substructures, to assess the feasibility of this potentially powerful technique. At the present, parametric lens models use well motivated scaling relations between mass and light to incorporate cluster member galaxies, and do not explicitly model line-of-sight structure. Here, we quantify modeling errors due to scatter in the cluster galaxy scaling relations and un-modeled line-of-sight halos. These errors are of the order of a few arcseconds on average for clusters located at typical redshifts ($z \sim 0.2-0.3$). Using Bayesian Markov Chain Monte-Carlo techniques, we show that the inclusion of these modeling errors is critical to deriving unbiased constraints on dark energy. However, when the uncertainties are properly quantified, we show that constraints competitive with other methods may be obtained by combining results from a sample of just 10 simulated clusters with 20 families each. Cosmography with a set of well studied cluster lenses may provide a powerful complementary probe of the dark energy equation of state. Our simulations provide a convenient method of quantifying modeling errors and assessing future strong lensing survey strategies.

Key words: cosmological parameters – gravitational lensing – clusters

1 INTRODUCTION

The recent influx of cosmological data from a variety of complementary observations has led to the development of a highly successful concordance cosmology. The overall picture that has emerged, where the most significant contributions to the Universe's energy content are baryonic matter (~ 5 per cent), non-relativistic dark matter (~ 20 per cent), and dark energy (~ 75 per cent), appears to be consistent with all current observations. A form of dark energy is required within the Friedmann-Robertson-Walker framework to explain the current epoch of accelerated expansion, which is most directly evident in the Hubble diagram of Type Ia supernovae (Riess et al. 1998; Perlmutter et al. 1999). However, a variety of other combined probes such as the Wilkinson Anisotropy Probe (WMAP) (e.g. Komatsu et al. 2010), baryon acoustic oscillations (Efstathiou et al. 2002; Seljak et al. 2005; Eisenstein et al. 2005) cluster abundances (Vikhlinin et al. 2009), cosmic shear measurements (Bacon et al. 2000; Kaiser et al. 2000; Van Waerbeke et al. 2000; Wittman et al. 2000; Semboloni et al. 2006), and cluster baryon fractions (Allen et al. 2004) also provide compelling evidence for its existence.

Dark energy is typically parameterized by an equation-of-state with the form $P = w_x \rho$, where $w_x < -1/3$ in the current epoch. Time variation or observed deviations from $w_x = -1$ at the present day could yield important clues to its nature. In the last decade, much effort has been devoted to further constraining the equation of state. Owing to the influence of systematic errors in astrophysical measurements, the development of complementary observational techniques is vital to this task. In this spirit, we investigate the use of cluster strong lensing (CSL) as a complementary technique to constrain w_x.

The possibility of constraining cosmology with CSL systems has been explored in the past (e.g. Paczynski & Gorski 1981; Link & Pierce 1998; Cooray 1999; Golse et al. 2002; Sereno 2002; Soucail et al. 2004; Dalal et al. 2005; Meneghetti et al. 2005a,b; Macciò 2005; Gilmore & Natarajan 2009; Jullo et al. 2010). The abundance of arcs may provide useful cosmological constraints. Meneghetti et al. (2005b) and Macciò (2005) explored the statistics of arcs in various dark energy cosmologies. They found that the variation in arc abundances, particularly at higher redshifts, can potentially be used to differentiate between dark energy models.

⋆ Email: anson.daloisio@yale.edu
† Email: priya.natarajan@yale.edu

The locations of images in CSL systems also contain useful cosmological information. These image positions depend not only on the mass distribution, but also on the angular diameter distances between the observer, lens, and source. If more than one set of images is observed, the geometrical dependence may be exploited to probe the cosmological parameters. In this paper we will explore the latter technique in greater detail.

Since the cores of clusters have surface densities which are typically much larger than the critical surface density for multiple image production, they are prime locations for identifying strongly lensed images. Indeed, cluster lenses containing an abundance of multiple images have already been utilized to place tight constraints on mass distributions in the inner regions of clusters. The most well studied CSL system to date is Abell 1689 (Broadhurst et al. 2005; Halkola et al. 2006; Limousin et al. 2007; Jullo et al. 2010). At present, strongly lensed images from 42 unique sources have been identified. Utilizing the large number of constraints and high resolution of the Hubble Space Telescope (HST) Advanced Camera for Surveys (ACS), the parametric mass models cited above can reproduce the observed image locations to within a few arcseconds. Similar, though less detailed, strong lensing analyses have been carried out for a growing sample of clusters (e.g. Natarajan et al. 2002; Kneib et al. 2003; Elíasdóttir et al. 2007; Limousin et al. 2008; Natarajan et al. 2009; Richard et al. 2009; Smith et al. 2009; Richard et al. 2010a,b).

Preliminary work has been done on bringing these rich systems to bear on cosmological parameters. Golse et al. (2002) explored simulated constraints on the mean matter density Ω_m and w_x using a single cluster with three strongly lensed sources. Sereno (2002) applied this technique to the cluster Cl0024+1654 at $z = 0.4$. Their results were found to be consistent with a flat, accelerating universe. Soucail et al. (2004) performed a more detailed application to Abell 2218 using only 4 multiple-image systems. Assuming a flat universe, their results are consistent with $\Omega_m < 0.3$ and $w_x < -0.85$. Most recently, Jullo et al. (2010) obtained $\Omega_m = 0.25 \pm 0.05$ and $w_x = -0.97 \pm 0.07$ by combining a strong lensing analysis of Abell 1689 with WMAP and X-Ray cluster constraints.

Theoretical investigations of this technique using simulations were performed by Dalal et al. (2005). They ray-traced through N-body simulations to create mock strong lensing image catalogs. They then attempted to recover the input cosmology by fitting a parametric NFW model and found that significant biases can result. Owing to the relatively large errors due to complexities in the mass distribution and line-of-sight (LOS) structure, they conclude that a single lensing system may not provide significant leverage on cosmological parameters.

Perhaps the most obvious way to overcome these difficulties is to obtain a larger sample of CSL systems. This approach has the advantage that results obtained from different lines of sight are statistically independent. Hence, their results may be combined in a trivial manner. More recently, Gilmore & Natarajan (2009) explored the prospect of **combining** CSL systems as a more powerful probe of dark energy. They found that competitive constraints can be obtained by combining at least 10 lenses with 5 or more image systems. Note that space-based measurements, with positional errors ~ 0.1 arcseconds, and spectroscopic redshift determinations ($\sigma_z \sim 0.001$) are a necessity. The current work expands upon the Gilmore & Natarajan (2009) investigation. We further explore the issue of overcoming large modeling uncertainties by combining a sample of CSL systems. We utilize more realistic simulations of cluster lensing systems that include sub-structure in the lens plane and line-of-sight structure to address several sources of modeling errors. Moreover, instead of a maximum likelihood routine, a Bayesian Markov Chain Monte-Carlo (MCMC) technique is used to probe the full parameter space, allowing us to marginalize over all lens parameters and draw more robust conclusions on the ability of CSL to constrain cosmological parameters.

This paper is organized as follows. In Section 2 we briefly discuss the sensitivity of CSL to cosmological parameters. In Section 3 we describe our simulations and discuss parameter recovery through Bayesian MCMC. In Section 4 we use our Monte-Carlo simulations to explore modeling uncertainties arising from complexities in the cluster galaxy population. We also perform a simple investigation of errors due to correlated LOS structure, and a more detailed analysis of uncorrelated LOS halos. In Section 5, we explore the prospect of overcoming these errors using a sample of 10 simulated clusters. We derive simulated constraints on the dark energy equation-of-state for this sample. In Section 6, we explore how differences in the large-scale mass distribution of the lens, including bi-modality, affect cosmological constraints. Finally, we offer concluding remarks in Section 7.

2 IMAGE LOCATIONS AND THE DARK ENERGY EQUATION-OF-STATE

In this section, we briefly outline the sensitivity of CSL to cosmological parameters. For a more detailed discussion, see Golse et al. (2002) and Gilmore & Natarajan (2009). The lens equation is given by

$$\vec{\beta_i} = \vec{\theta_i} - \frac{2}{c^2}\frac{D_{ls}}{D_l D_s}\nabla\phi(\vec{\theta_i}), \quad (1)$$

where the angular coordinates of the source i and its corresponding image(s) are given by $\vec{\beta_i}$ and $\vec{\theta_i}$ respectively, and ϕ is the projected Newtonian potential of the lens. For the parametric models used in this work, the potential is typically normalized by the associated central velocity dispersion, σ_v. The subscripts o, l, and s correspond to the observer, lens, and source. We define D_{ab} to be the angular diameter distance from z_a to z_b. In the case of a flat, two-component universe, D_{ab} is given by

$$D(z_a, z_b) = \frac{c/H_0}{1+z_b}\int_{z_a}^{z_b} \mathrm{d}z \ \left(\Omega_m(1+z)^3 + \Omega_X(z)\right)^{-1/2}, \quad (2)$$

where H_0 is the present day Hubble constant, c is the speed of light, and Ω_m is the present day matter density normalized by the critical density. The function $\Omega_X(z)$ is the contribution from dark energy and its form depends on the choice of parameterization. In this work we consider two parameterizations: 1) a constant equation of state, w_x. 2) the widely used Chevallier, Polarski, and Linder (CPL) parameterization, $w_x(z) = w_0 + w_a z/(1+z)$ (Chevallier & Polarski 2001; Linder 2003). In this case, $\Omega_X(z)$ is given by

$$\Omega_X(z) = \Omega_X(1+z)^{3(1+w_0+w_a)}\exp\left[-\frac{3w_a z}{1+z}\right]. \quad (3)$$

Note that the angular diameter distance factor in (1) contains all of the explicit dependence on the cosmological parameters, while the influence of the mass distribution comes in through the gradient term. The CSL technique discussed in this paper is a purely geometric probe and utilizes only the angular diameter distances for constraints. Aside from the abundance of image systems, the influence of cosmology on the detailed properties and formation of lensing structures does not come into play.

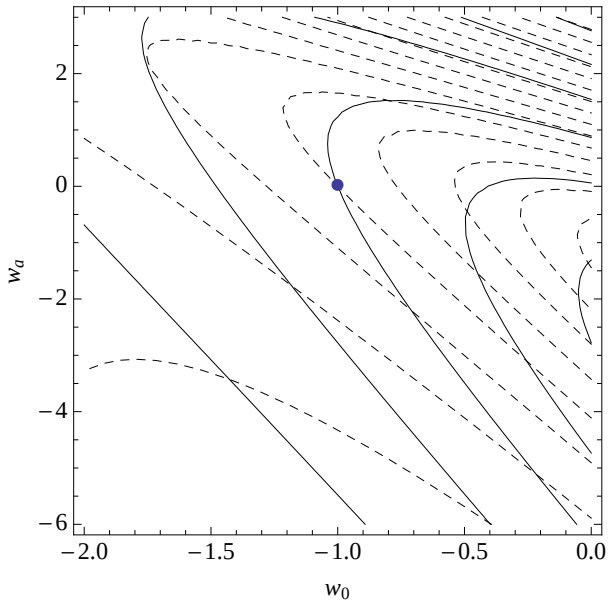

Figure 1. Contours of the ratio $\Gamma^{(1)}/\Gamma^{(2)}$ in the $w_0 - w_a$ plane for lensing configurations with two multiply-imaged families from background galaxies at 2 distinct redshifts. The solid (dashed) curves correspond to $z_l = 0.2(0.3)$, $z_{s1} = 0.7(1.0)$, and $z_{s2} = 1.5(4)$.

Consider a single source at $\vec{\beta}_i$ that is lensed into a set of n multiple images $\vec{\theta}_{i,j}$, where $j = 1, ..., n$. In this case, it is impossible to isolate the effect of the cosmological parameters because the geometric factor in equation (1) is completely degenerate with the normalization of the projected lens potential. If more than one source is lensed into multiple image families, as is typically the case in CSL systems, then the above degeneracy is broken. Consider the case of N sources at different redshifts. In this case, there is a set of N lens equations, each given by

$$\begin{aligned} \vec{\beta}_1 = &\quad \vec{\theta_1} - \tfrac{2}{c^2}\Gamma^{(1)}\nabla\phi(\vec{\theta_1}) \\ \vdots &\quad \vdots \\ \vec{\beta}_N = &\quad \vec{\theta_N} - \tfrac{2}{c^2}\Gamma^{(N)}\nabla\phi(\vec{\theta_N}), \end{aligned} \tag{4}$$

where the Γ's represent the geometric factors. The superscripts on Γ denote the different source redshifts. Note that equation (4) applies to a single cluster lens so that the normalization of ϕ is the same for each line. Owing to the N different source redshifts involved, a change of the cosmological parameters may now be discerned from changes in σ_v. Hence the dark energy equation-of-state may be probed using a set of multiply imaged systems as constraints.

It is instructive to consider the simple example of a lens at z_l and two families at z_{s1} and z_{s2}. In this case, the two lens equations may be combined by eliminating the normalization of ϕ. The effective dependence on cosmology for the system is through the ratio $\Gamma^{(1)}/\Gamma^{(2)}$. Figure 1 shows contours of $\Gamma^{(1)}/\Gamma^{(2)}$ in the $w_0 - w_a$ plane (CPL model) for two different lensing configurations (for the constant w_x case, see Gilmore & Natarajan 2009). The solid (dashed) curves correspond to $z_l = 0.2(0.3)$, $z_{s1} = 0.7(1.0)$ and $z_{s2} = 1.5(4)$. The contours, which correspond to one per cent differences in the geometric ratios, illustrate degeneracies in the $w_0 - w_a$ plane for CSL cosmography with two families. Degeneracies may be broken by using a variety of lensing configurations with different lens and source redshifts.

3 METHODS

3.1 Simulations of Cluster Strong Lenses

In this section, we describe how our Monte-Carlo simulations of cluster lenses are generated. In the bulk of this work, we employ simulated clusters with two components: 1) a smooth large-scale density profile. 2) galaxy sized sub-structures within the core of the cluster. Lenses with more complicated large-scale components are known to exist (for example, see Limousin et al. 2007; Jullo & Kneib 2009). We also address cluster bi-modality in Section 6.

We model all cluster and galaxy scale halos with a smoothly truncated version of the Pseudo-Isothermal Elliptical Mass Distribution (PIEMD) in Kassiola & Kovner (1993) (see Kneib et al. 1996). The profile is characterized by a central velocity dispersion σ_v, core radius $r_{\rm core}$, scale radius $r_{\rm cut}$, and ellipticity parameter ϵ. In addition, the profile center (x_0, y_0) and position angle $\theta_{\rm PA}$ are used to characterize lens the orientation. For the circular case, $r_{\rm core}$ marks the transition from a constant density to $\rho \sim r^{-2}$. Outside of $r_{\rm cut}$, the density drops off rapidly as $\rho \sim r^{-4}$. The truncated PIEMD profile has been used to successfully model both cluster and galaxy scale lenses in the past (e.g., Natarajan et al. 1998, 2002; Limousin et al. 2007).

The first step in simulating a lensing configuration is to create a smooth, cluster-sized halo. The parameters σ_v, $r_{\rm core}$, and $r_{\rm cut}$ are drawn uniformly from the intervals $1000 - 1500$ km/s, $30 - 100$ kpc, and $800 - 1000$ kpc respectively. An ellipticity and position angle are randomly assigned in the intervals $0 - 0.3$ and $0 - 360$ degrees. The halo center is fixed at the origin. A cluster redshift in the range $z = 0.025 - 0.6$ is drawn from the distribution in Gilmore & Natarajan (2009), which was derived from the MAssive Cluster Survey (Ebeling et al. 2001)[MACS]. In this work, we do not take into account the effects of dark energy on cluster assembly characteristics. We note that a change in cluster properties, such as an increase in their concentrations as indicated in Grossi & Springel (2009) for example, could certainly affect the number of multiple-image families and multiplicities observed. However, we emphasize that the CSL technique utilized here is purely geometric in nature, and does not rely on cluster properties to constrain dark energy.

Galaxy-scale potentials are incorporated into the simulated clusters with the mean scaling relations derived empirically from observations,

$$\sigma_v = \sigma_v^* \left(\frac{L}{L^*}\right)^{1/4} \tag{5}$$

$$r_{\rm cut} = r_{\rm cut}^* \left(\frac{L}{L^*}\right)^{1/2}, \tag{6}$$

where L is the galaxy luminosity. Scaling relations such as these are typically used to model galaxy halos in parametric analyses. The scaling of the velocity dispersion with luminosity is motivated by the Tully-Fisher and Faber-Jackson relations for spiral and elliptical galaxies respectively. We fix the core radii of all galaxy sub-halos to be vanishingly small so that the density profiles are approximately isothermal ($\rho \sim r^{-2}$) inside of the scale radii. Although it is sensitive to the mass of sub-halos, cluster strong lensing is at present unable to distinguish between different profile shapes for small-scale structures (Natarajan et al. 2002, 2009).

In order to account for cluster-to-cluster variation in the galaxy scaling relations, for each lens we draw σ_v^* and $r_{\rm cut}^*$ from Gaussian distributions with mean values $\bar{\sigma}_v^* = 200$ km/s, $\bar{r}_{\rm cut}^* = 40$ kpc. The standard deviations for the σ_v^* and $r_{\rm cut}^*$ distributions

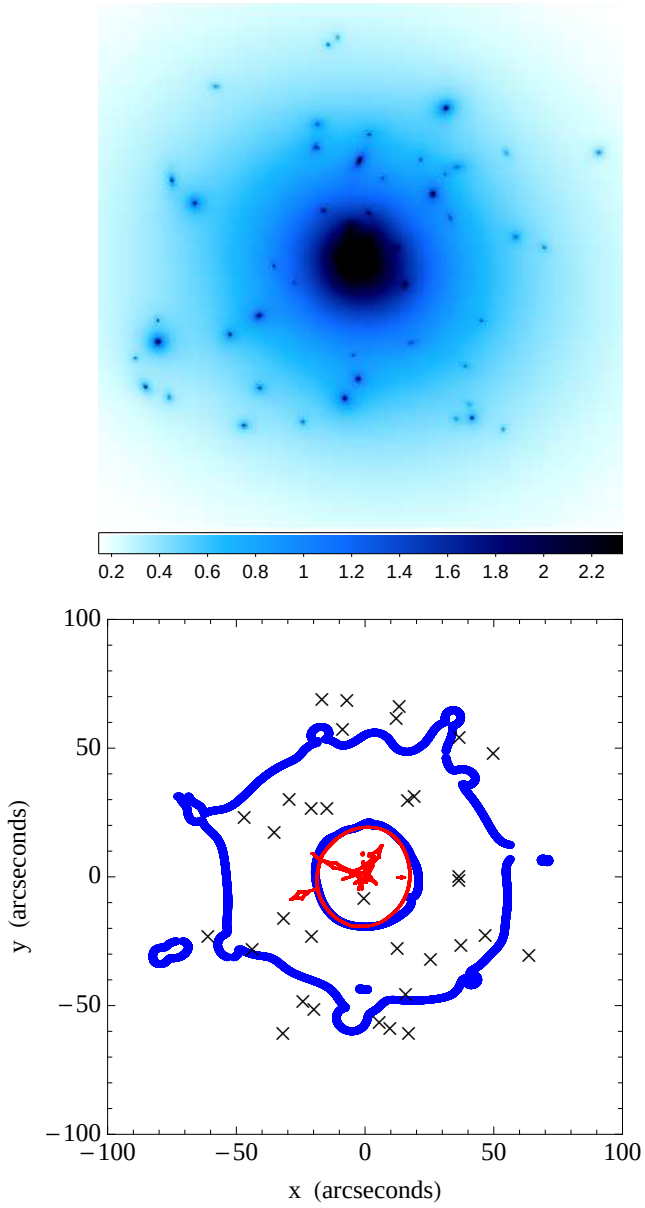

Figure 2. A simulated lensing configuration with 20 multiply imaged families. Top panel: a convergence map of the lensing cluster with $z_l = 0.24$ and $z_s = 1.5$. The size of the frame is 200×200 arcseconds^2. Bottom panel: the image positions, shown as x's, and the critical curves and caustics for $z_s = 1.5$. The location and redshifts of images from sources lying between $z_s \sim 0.5 - 5$ are used to simultaneously invert the lens and constrain the dark energy equation-of-state.

are 40 km/s and 15 kpc respectively, in accordance with observational lensing studies (Natarajan et al. 2002). For each galaxy, we first draw an I-band absolute magnitude in the range $M_I = -18$ to $M_I = -23$ from a Schechter function with $M_I^* = -21.7$ and $\alpha = -1.3$, consistent with recent cluster observations (e.g. Harsono & De Propris 2009). The PIEMD parameters σ_v and $r_{\rm cut}$ are then calculated using (5) and (6). In section 4, we will draw individual σ_v and $r_{\rm cut}$ values from Gaussian distributions to account for scatter in the scaling relations (5) and (6). We uniformly draw a position angle and an ellipticity in the interval $\epsilon = 0 - 0.75$. Finally, a galaxy position is drawn from the cluster-scale PIEMD density profile. We place all galaxies within 300 kpc of the cluster center. In addition to 50 galaxies, for each cluster we draw M_I between $M_I = -23$ and $M_I = -24$ from the above Schechter function for the Brightest Cluster Galaxy (BCG). For simplicity, we use the same scaling relations for the BCG as the other cluster galaxies to assign the corresponding σ_v and $r_{\rm cut}$. The BCG position is drawn from a uniform distribution within a radius of 50 kpc from the cluster center. The BCG σ_v and $r_{\rm cut}$ parameters are left free during parameter recovery.

The next step is to randomly draw a unique distribution of background galaxies to be lensed by each cluster. We use the redshift distribution obtained by Gilmore & Natarajan (2009) from the WFPC2 Hubble Deep Field and Hubble Deep Field-South photometric redshift catalogues (Fernández-Soto et al. 1999; Yahata et al. 2000). We create a population of background galaxies by drawing redshifts and AB(8140) apparent magnitudes in the ranges of $z = 0.4 - 5.0$ and $M_{AB}(8140) = 19 - 28$ respectively from this distribution. The galaxy positions are drawn uniformly in the field of view. The background galaxy number density is fixed to 215 arcmin^{-2} in accordance with the Hubble Deep Field as in Gilmore & Natarajan (2009).

After drawing cluster and source properties we lens the population of background galaxies. We apply a magnitude cut of $M_{AB}(8140) = 24.5$ to remove simulated images that are in practice too dim to obtain accurate spectroscopic redshifts. We then sort the images into multiple-image families, which consist of at least two detectable images. The rest of the images are discarded. The positions and redshifts of the final families constitute a fiducial catalogue of constraints for the lensing system. In Section 4, we will explore perturbations to the catalogs due to complexities in the cluster galaxy population and LOS structure.

Figure 2 shows an example of a lensing configuration generated by the above procedure. The top panel shows the convergence map of a cluster at $z_l = 0.24$ with $z_s = 1.5$, illustrating the smooth cluster component and 51 core cluster galaxies. The field of view is 200 by 200 arcseconds^2, consistent with an ACS image. The bottom panel shows the corresponding critical curves and caustics for $z_s = 1.5$. The panel also shows the image positions for 20 strongly lensed sources with redshifts ranging from $z_s = 0.87$ to $z_s = 3.4$.

3.2 Bayesian MCMC

We use the Bayesian MCMC sampler in the LENSTOOL software[1] for parameter recovery. In this section we provide a brief summary of the technique. More details can be found in Jullo et al. (2007). LENSTOOL is employed to map image locations to the source plane and vice versa using equation (1) for a given lens configuration. An image plane χ^2 statistic may be computed from

$$\chi^2_I = \sum_{f=1}^{N_f} \sum_{i=1}^{n_f} \left(\vec{\theta}_{fi} - \vec{\theta}^{\rm mod}_{fi}\right)^T C^{-1}_{fi} \left(\vec{\theta}_{fi} - \vec{\theta}^{\rm mod}_{fi}\right) \quad (7)$$

where $\vec{\theta}_{fi}$ and $\vec{\theta}^{\rm mod}_{fi}$ are the observed and model positions of image i of family f respectively and C is the corresponding covariance matrix. Working in the image plane, particularly in the case where a large number of χ^2 are computed, is time consuming due to the fact that the lens equation must be inverted. A less computationally expensive approach is to linearize the lens equation and rewrite equation (7) in terms of source plane quantities. In this case,

[1] http://www.oamp.fr/cosmology/lenstool

$$\chi^2_S = \sum_{f=1}^{N_f} \sum_{i=1}^{n_f} \left(\vec{\beta}_{fi} - \left\langle \vec{\beta}_f \right\rangle\right)^T M^T C_{fi}^{-1} M \left(\vec{\beta}_{fi} - \left\langle \vec{\beta}_f \right\rangle\right), \quad (8)$$

where M is the magnification tensor, $\vec{\beta}_{fi}$ is the source plane position, and $\left\langle \vec{\beta}_f \right\rangle$ is the barycenter of family f. In the source plane approach, the models with the lowest χ^2 are the those in which source plane positions from the same family exhibit minimal scatter. It is often the case that some images in a family go undetected due to obstruction or demagnification. Note that the location of *all* images in a given family is not required. We only require the identification of more than one image in a family.

The parameters in the models used for the MCMC are summarized in Table 1. We use flat 50 per cent priors, centered on the input values, for all mass profile parameters, except for the cluster center, which we limit to ± 10 arcseconds. Our results are insensitive to the width of the cluster center limits. For simplicity, we assume that mass traces light for the cluster galaxies, and fix their positions. In the case of constant equation-of-state, we assume flat priors of $0 < \Omega_m < 0.7$ and $-2 < w_x < 0$. For the CPL parameterization, we assume flat priors of $-3 < w_0 < 0$ and $-6 < w_a < -w_0$. We also assume $0 < \Omega_m < 0.7$. In practice, the exclusion of $w_a > -w_0$ would come from higher redshift constraints (see Kowalski et al. 2008). The CPL parameterization approaches $w_0 + w_a$ as $z \to \infty$. Hence models above the $w_a = -w_0$ line have $w_x > 0$ at high redshifts, implying that dark energy dominates at early times. Current results favor dark energy making up only a small fraction of the total energy density for $z \gg 1$ (e.g. Kowalski et al. 2008; Komatsu et al. 2010).

The MCMC sampler works by randomly drawing parameter sets from Table 1. The χ^2 is computed using the simulated position and redshift data and each model is either accepted or rejected using a variant of the Metropolis-Hasting algorithm. As the process is repeated, the sample of points in the parameter space converges to the posterior probability density function (PDF). To avoid getting stuck in local maxima, the MCMC sampler in LENSTOOL utilizes the convergence technique of selective annealing. Following Jullo et al. (2007), we use a convergence rate of 0.1 and fix the number of samples to be $50,000$.

Table 1. Free parameters in the Bayesian MCMC sampler.

Cluster-scale parameters	Description
x,y	Center of the cluster density profile
σ_v	Central velocity dispersion
$r_{\rm core}$	Core radius
$r_{\rm cut}$	Scale radius
ϵ	Ellipticity
$\theta_{\rm PA}$	Position angle
BCG	
$\sigma_v, r_{\rm cut}$	Velocity dispersion and scale radius of the brightest cluster galaxy
Galaxy-scale	
$\sigma_v^*, r_{\rm cut}^*$	Normalization of the scaling relations (5) and (6)
Cosmological	
Ω_m	Mean matter density
w_x	Dark Energy equation-of-state
or	
w_0,w_a	

4 MODELING ERRORS IN CSL

4.1 Effect of cluster galaxies

The inclusion of galaxy-scale potentials in cluster lens models greatly improves their ability to reproduce observed images. In some cases, individual cluster galaxies can have a large impact on the configuration of images, and it may difficult to reproduce observations without modeling them individually (for example, when the presence of a cluster galaxy changes the multiplicity of images). However, regarding the bulk of the galaxy population, one is forced to make some simplifying assumptions owing to the limited number of constraints and large number of parameters required. Specifically, the velocity dispersion and scale radii parameters are typically assumed to follow empirically motivated scaling relations such as (5) and (6). In this section we examine the effect that these simplifying assumptions have on our ability to reproduce image locations.

It is well known that the Faber-Jackson and Tully -Fisher relations exhibit considerable scatter. We should therefore expect significant scatter in the scaling of σ_v with luminosity. It is also reasonable to expect a similar degree of scatter in the $r_{\rm cut}$ relation. The deviations of individual cluster galaxies from the relations can introduce perturbations to nearby images which cannot be accounted for with a simple parametric model. We should not expect our models to reproduce images to within this perturbation scale. We perform simple Monte-Carlo simulations to quantify these deviations.

For each of our simulated lensing configurations, we draw 1000 different galaxy populations. We randomly draw velocity dispersions σ_v and scale radii $r_{\rm cut}$ from Gaussian distributions with mean values obtained through (5) and (6) in the fiducial models. We use standard deviations of 10, 20, and 30 per cent of the mean to explore how varying degrees of scatter affect image positions. We lens the given source catalog through each realization and examine the scatter in image positions. Figure 3 shows results from one such lensing configuration. Each point corresponds to an image in one realization of the Monte-Carlo simulations. The open circles indicate the position of cluster galaxies. The tangential shapes of the image distributions illustrate that the deviations are generally larger along the local principal magnification direction.

In the top panel of Figure 4, we compute image deviations relative to the fiducial models with no scatter in the cluster galaxies, and show the probability density of these deviations. The solid, dashed and dot-dashed histograms correspond to 10, 20, and 30 per cent scatter respectively. Since each simulated cluster in our sample is at a different redshift, we calculate the deviations in comoving $\rm kpc$. The average deviation in each case is 2.5, 4.9 and 6.9 comoving $\rm kpc$ respectively. This corresponds to 0.6, 1.3, and 1.8 arcseconds for clusters at $z \sim 0.2$ respectively. In rare cases, deviations can be as large as ~ 10 arcseconds.

We now turn our attention to the effect of the power law indices in equation (5) and (6). Although these relations have been successfully used in the past for constraining the mass distributions of cluster lenses, we examine here more closely the implications of these assumptions. As discussed above, the scaling of σ_v with $\sim L^{1/4}$ is motivated by well established empirical results. However, while σ_v itself is not directly measured observationally, studies of individual galaxy lenses from the SLACS survey for instance (see Bolton et al. 2008; Barnabè et al. 2009) suggest that the mea-

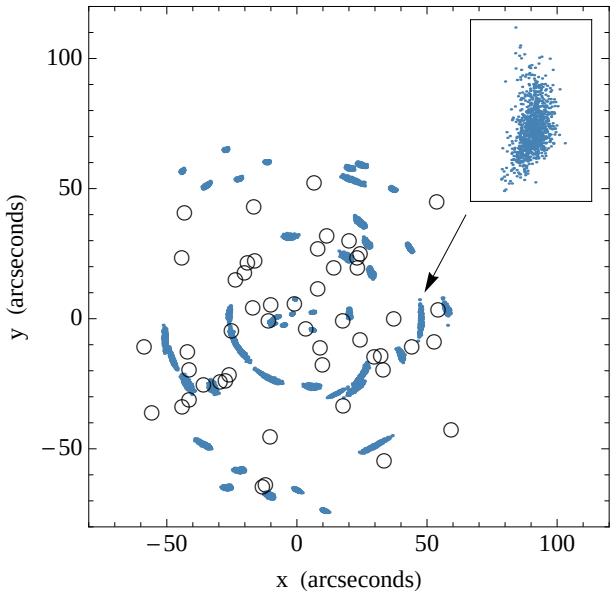

Figure 3. Results from a Monte-Carlo simulation of CSL illustrating the effect of scatter in cluster galaxy scaling relations. We show the lensed image locations obtained from 1000 random realizations of the cluster galaxy population for $z_l = 0.34$. A 20 per cent scatter in the scaling of velocity dispersion and scale radius with luminosity is assumed. The open circles show the location of cluster galaxies. The inset (6×16 arcseconds^2) shows the Monte-Carlo realizations for a single image. Each point corresponds to the location of the lensed image for a particular realization of the cluster galaxy population.

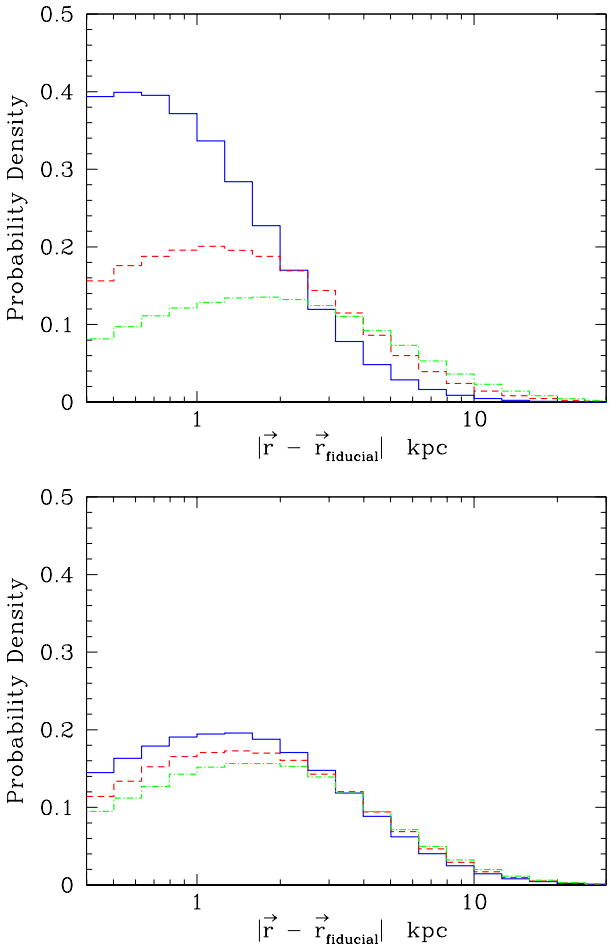

Figure 4. Top panel: magnitude of image deviations, in comoving kpc, between models with and without scatter in the cluster galaxy scaling relations. For the models with scatter, velocity dispersions and scale radii are drawn from Gaussian distributions with mean given by equations (5) and (6). To illustrate the effect of varying degrees of scatter, we assume standard deviations of 10, 20, and 30 per cent of the mean values for the solid, dashed, and dot-dashed histograms respectively. The scale of these perturbations is used to quantify modeling errors that arise from complexities in the cluster galaxy population. Bottom panel: deviations due to variation in the slope of the scaling relations, with a fixed 20 per cent scatter in the σ_v and $r_{\rm cut}$ values. Assuming mean values of $1/4$ and $1/2$ respectively, power-law indices for equations (5) and (6) are randomly drawn. The indices have a minimal effect due to the scatter in σ_v and $r_{\rm cut}$.

sured stellar velocity dispersion within an effective radius is a good proxy for the velocity dispersion of the lensing mass model. Owing to a lack of empirical data, the assumed scaling of $r_{\rm cut}$ with luminosity is more uncertain and may vary considerably.

To determine the effect of assuming an incorrect scaling with luminosity, we again perform Monte-Carlo simulations. For each cluster in our sample, we draw 1000 realizations where we vary the power-law indices. We draw from a Gaussian with mean given by $1/4$ (σ_v) and $1/2$ ($r_{\rm cut}$). We again use standard deviations of 10, 20, and 30 per cent of the mean to explore the effect of various amounts of scatter. We assume a fixed scatter in the σ_v and $r_{\rm cut}$ values themselves of 20 per cent. The bottom panel of Figure 4 shows image deviations with respect to the fiducial models in which there is no scatter in the scalings whatsoever. The 10, 20, and 30 per cent cases are shown. We note that varying the power law indices has only a mild effect on the deviations if there is scatter present in the values themselves. The effect of the indices is essentially lost in the scatter.

Finally, we have checked that the above deviations are relatively independent of the cosmology, varying only by a few per cent for a wide range of Ω_m and w_x parameters.

4.2 The effect of line-of-sight halos

4.2.1 The multiple lens plane approximation

The thin-lens approximation, equation (1), applies to the case where the lensing mass distribution is localized. In this case, the deflection angle may be approximated as a single impulse. However, in cosmological applications, light from distant sources may be deflected by many structures along the path to the observer. The matter distribution may be broken up into multiple lens planes so that the deflection angle is approximated by a series of impulses. In this case, the angular position of the light ray at lens plane j is given by

$$\vec{\theta}_j = \vec{\theta}_1 - \sum_{i=1}^{j-1} \frac{D_{ij}}{D_j}\, \hat{\alpha}\left(\vec{\theta}_i\right), \tag{9}$$

where $\vec{\theta}_1$ is the observed image position and $\hat{\alpha}\left(\vec{\theta}_i\right)$ is the deflection angle evaluated at the ray position on plane i (see Schneider et al. 1992, for example). Note that the lens plane iterator increases with distance from the observer. Equation (9) may be iterated to trace an image location back to the appropriate source plane.

Following Hilbert et al. (2009), we use a quicker and more computationally efficient alternative to equation (9), where the ray position on plane j is written in terms of the positions on lens planes $j-1$ and $j-2$,

$$\begin{aligned}\vec{\theta}_j &= \left(1-\frac{f_K^{(j-1)}}{f_K^{(j)}}\frac{f_K^{(j-2,j)}}{f_K^{(j-2,j-1)}}\right)\vec{\theta}_{j-2} \\ &+\frac{f_K^{(j-1)}}{f_K^{(j)}}\frac{f_K^{(j-2,j)}}{f_K^{(j-2,j-1)}}\vec{\theta}_{j-1} \\ &-\frac{f_K^{(j-1,j)}}{f_K^{(j)}}\hat{\alpha}\left(\vec{\theta}_{j-1}\right).\end{aligned} \tag{10}$$

Here, f_K is the comoving angular diameter distance, $f_K^{(a,b)} \equiv D(z_a, z_b)/(1+z_b)$.

We developed our own software to perform the ray tracing calculations in the following sections. At present, the code can perform ray tracing through planes consisting of lenses with analytic mass profiles, such as the PIEMD and NFW profiles. For the task of obtaining image locations, the code traces grid points backwards to the appropriate source redshift using equation (10). The set of transformed grid points in the source plane is then divided into triangles (c.f. Schneider et al. 1992). The triangles enclosing the source are identified and refined by repeatedly shrinking their sizes to improve the resolution of the image location.

4.2.2 Correlated halos

In this section, we explore the impact of structures situated along the line-of-sight in cluster strong lensing systems. We begin by considering, in a simplified manner, the effects of correlated structures. In the next section, we will consider uncorrelated halos in the light cone.

All CSL studies to date have utilized a single lens plane for mass modeling. In what follows, we ask whether correlated structures can be reasonably modeled on the same redshift plane as the cluster, or whether models consisting of multiple lens planes are necessary. We consider the simple example of a cluster lens with an infalling group-sized halo residing slightly behind it. Due to its proximity, the projection might result in the association of the group-sized halo with the cluster system. We simulate a cluster at $z = 0.192$ with an aperture mass of $M = 9.5 \times 10^{14}\ \mathrm{M}_\odot$ within a radius of 1 Mpc. The cluster has 40 core galaxies containing a total mass of $2 \times 10^{13}\ \mathrm{M}_\odot$. The infalling group, with an aperture mass of $6.3 \times 10^{13}\ \mathrm{M}_\odot$, is located 20 comoving Mpc behind the cluster at a redshift of $z = 0.198$, and is situated at $(x, y) = (40, 40)$ arcseconds with respect to the cluster center. We associate 10 galaxies with the group.

We randomly draw 20 different source catalogs with source redshifts between $z \sim 0.7 - 5$ and lens them with the two-plane model. Multiply imaged systems are identified and selected. To test the effect of using only one lensplane to model the system, we create a model in which the group-sized halo and associated galaxies reside on the same lensplane as the cluster. We lens the same 20 catalogs and compare image locations.

We find the mean deviation between the two catalogs to be 0.26 arcseconds, with largest deviations of ~ 1 arcsecond. Such cases are rare - $87(97)$ per cent of deviations are less than $0.5(1)$ arcseconds - and typically occur for images located close to the group-sized halo. We also tested a single lensplane model which is located halfway between the cluster and group-sized halo. We found almost no difference in the deviations. Based on the magnitude of deviations, we conclude that in the case where there is a dominant lensing system in mass, one can reasonably use a single lensplane model. Such an approach may introduce modeling errors which are typically on the order of a few tenths of an arcsecond. However, we note that these effects are subdominant to the effects of scatter in the cluster galaxy population, as shown in the last section. Moreover, in the next section, we will show that the effects of uncorrelated galaxy-scale halos along the line-of-sight are greater.

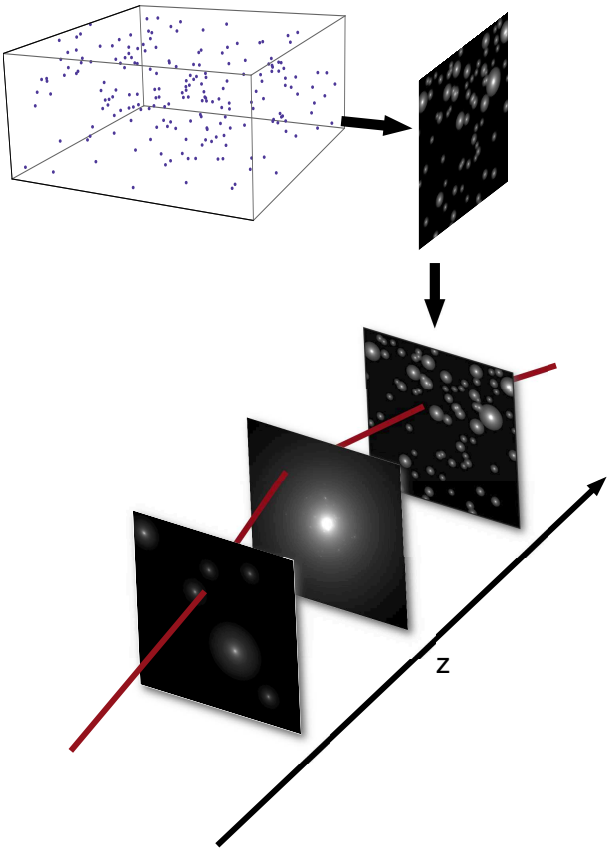

Figure 5. Schematic diagram illustrating the creation of lensplanes to quantify the effects of LOS halos. A rectangular slice of the Millenium Simulation box is taken. The locations of halos are projected along the long axis and analytic NFW potentials are placed on those sites. The NFW parameters are obtained through scaling relations with mass and redshift. The lensplane is inserted at the appropriate redshift and a multi-plane lensing algorithm is used to trace rays. In this work, forty-two lensplanes are used between $z = 0$ and $z = 5$.

We now consider the case when the masses of the two line-of-sight structures are roughly equivalent. We set the mass of the two halos to $4.5 \times 10^{14}\mathrm{M}_\odot$ and lens the 20 source catalogs again. The deviations increase to 0.91 arcseconds on average and can be as high as a few arcseconds. We conclude that in the case with two equal-sized halos, it may be necessary to utilize two lensplanes in order to minimize modeling errors.

We note that the above investigation is limited due to the simplified parametric models used. Galaxy clusters are typically part of a rich network of structures which cannot be fully captured in the approach we have taken. To test these effects in a more realistic way, including larger-scale structures such as filaments, it is best to utilize particle data from a cosmological N-body simulation. How-

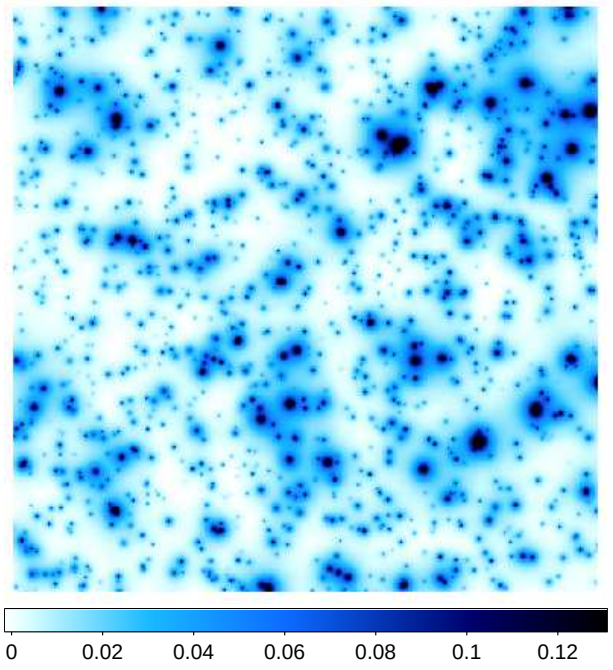

Figure 6. Example convergence map of a simulated line-of-sight created from Millenium Simulation halo catalogs, for $z_s = 1.5$. The field of view is 400×400 arcseconds^2. For each simulation snapshot, a lensplane is created by projecting halo locations and placing analytic NFW potentials. The NFW parameters are obtained through scaling with the mass and redshift of the halo. We use many line-of-sight realizations such as the above to calculate perturbations from the cluster-only model, and quantify modeling errors.

ever, such an investigation is beyond the scope of the current work, and we defer to a future paper.

4.2.3 Uncorrelated halos

We now turn our attention to the influence of uncorrelated galaxy-scale halos along the line-of-sight. Although direct modeling of LOS halos from observations may ultimately improve the fit to images, perhaps a more practical approach at the present is to quantify the errors due to neglecting them in the lens model. We utilize halo catalogs from the Millennium Simulation Database[2] (Springel et al. 2005) and the multiple-lensplane approximation (see Schneider et al. 1992, for example). A schematic of the procedure is shown in Figure 5.

We create one lensplane for each snapshot between $z = 0$ and $z = 5$, yielding a total of 42 planes. For each lensplane, we take a randomly oriented 3-dimensional slice of the corresponding snapshot (see Figure 5 for an illustration). The slices are rectangular with length equal to $\{r_{\rm com}(z_{i-1}, z_i) + r_{\rm com}(z_i, z_{i+1})\}/2$, where z_i is the redshift of snapshot i and $r_{\rm com}(z_a, z_b)$ is the comoving distance between z_a and z_b. The widths are chosen so that each plane fills a 400×400 arcsecond^2 area after projection. The locations of all halos above a threshold of 10^{11} $M_\odot$ in the slices are projected along the long axis. The masses and redshifts in the catalog are used to obtain mean concentration parameters through scaling relations obtained by Gao et al. (2008). In order to account for scatter about

[2] http://www.mpa-garching.mpg.de/millennium/

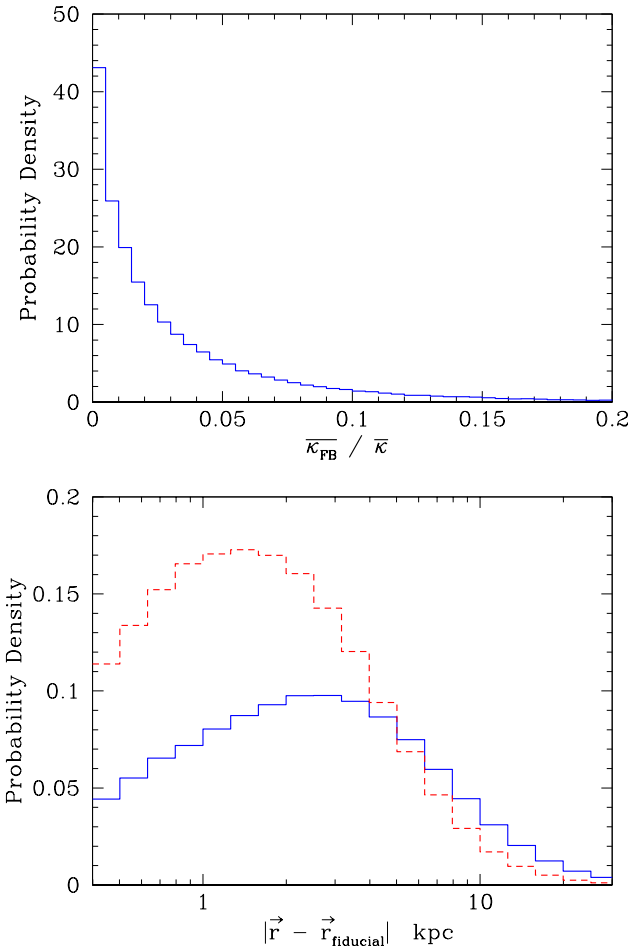

Figure 7. Top panel: ratio of LOS convergences excluding ($\bar{\kappa}_{\rm FB}$) and including ($\bar{\kappa}$) the contribution from the cluster plane. The contribution from foreground and background halos to the total LOS convergence is typically less than ~ 10 per cent. Bottom panel: the solid histogram shows image deviations, in comoving kpc, between the full light-cone and cluster only models. For reference, the dashed histrogram shows the cluster galaxy result for 20 per cent scatter in the scaling relations (see Figure 4). Uncorrelated LOS halos perturb image locations by ~ 9 kpc on average, corresponding to 2.3, 1.6, and 1.2 arcseconds at $z = 0.2$, 0.3 and 0.4 respectively.

these relations, we draw concentrations from a log-normal distribution with standard deviation given by 0.14 (Neto et al. 2007). Circularly symmetric NFW potentials with the corresponding parameters are then placed at the location of each halo. Since the mass of the NFW profile is not convergent, we truncate each profile at the virial radius (for lensing properties of the truncated NFW profile, see D'Aloisio et al. 2008). A typical convergence map for a simulated LOS, without cluster, is shown in Figure 6.

Since the slices are much smaller than the Millennium Simulation box, we can perform the above procedure many times for each lensplane to create an ensemble. We create random LOS realizations in order to quantify the modeling errors through a Monte-Carlo approach. We find that 500 LOS realizations are sufficient for numerical convergence. For each lensing configuration in our cluster sample, we lens the source catalogs through 500 LOS realizations with the cluster model placed at the appropriate redshift. We utilize a ray tracing code that we developed for this purpose.

Following Hilbert et al. (2007), we calculate the "LOS convergence" $\bar{\kappa}$ in order to quantify the lensing effect of the LOS halos. Note that this is not equivalent to the multi-plane generalization of the convergence, but is nonetheless useful for quantifying the effects of LOS structure. We ray trace each image in our simulations backwards to their respective source planes. We sum the surface mass densities weighted by the appropriate lensing efficiencies at each point along the trajectory. We do not subtract off the mean density of each plane. For each lensing system, we do this for all 500 LOS realizations. We calculate the LOS convergence including ($\bar{\kappa}$) and excluding ($\bar{\kappa}_{\rm FB}$) the contribution from the cluster plane. The top panel of Figure 7 shows the distribution of $\bar{\kappa}_{\rm FB}/\bar{\kappa}$ values. The contribution of foreground and background halos to the LOS convergence is typically less than ~ 10 per cent.

The LOS halos perturb the image locations in a manner similar to the results shown in Figure 3, though to a larger extent. We note that, in some cases, LOS halos can change the multiplicity of images. We compare the results of the LOS Monte-Carlo simulations to the image catalogs in the cluster-only cases. The solid histogram in the bottom panel of Figure 7 corresponds to deviations between the full LOS and cluster-only cases. For reference, the dashed histogram shows the case of 20 per cent scatter in the cluster galaxy σ_v and $r_{\rm cut}$ parameters (see the top panel of figure 4). Figure 7 indicates that the uncorrelated halos in the LOS perturb image locations by ~ 9 comoving kpc on average (corresponding to 2.3, 1.6, and 1.2 arcseconds at z = 0.2, 0.3, and 0.4 respectively).

5 SIMULATED CSL CONSTRAINTS ON DARK ENERGY

Having explored some of the most significant sources of error in CSL, we now use our simulations to perform a feasibility test on whether CSL systems with perturbations due to the LOS and cluster galaxy populations can yield useful dark energy constraints. We use the set of ten simulated clusters with 20 families each discussed above. Each cluster is placed within an independent light cone generated from the Millennium Simulation halo catalogs (see Section 4.2.3). The 50 core galaxies for each cluster are simulated with a 20 per cent scatter in the luminosity scaling relations (see Section 4.1). Since we have shown that variation in the power-law indices of equations (5) and (6) makes little difference in the image perturbations when there is significant scatter in the galaxy population, we fix them to the input values.

We first ray trace the sources through the LOS and cluster lensplanes to obtain a catalog of image positions. In order to obtain observed positions, we must account for the fact that light from the cluster itself is deflected by intervening matter. We therefore lens the cluster center through the lensplanes between the cluster and the observer, and calculate the image positions with respect to this center. We also include the effect of lensing on cluster galaxy positions and magnitudes. Finally, image positions are randomly shifted by ± 2 pixels (0.05 arcseconds per pixel) in order to roughly simulate space-based observational errors. We also redraw the source redshifts from normal distributions with variance equal to 0.001 to simulate measurement errors in spectroscopic redshifts. The final catalog of image positions and redshifts of strongly lensed sources constitutes the only set of constraints used in parameter recovery.

We estimate the total errors for each constraint using the Monte-Carlo simulations in the last section. Since the Monte-Carlo realizations tend to be distributed along the local principal magnification axis, for each image we transform to the coordinate system in which the magnification tensor is diagonal. In this coordinate system, the distribution is typically well approximated by a bi-variate normal distribution with zero correlations. Note that, in addition to the errors, the numerator of each χ^2 contribution is calculated in the transformed coordinate system during parameter recovery. Modeling errors due to the LOS halos, scatter in cluster galaxy scaling relations, and an observational error of 0.1 arcsecond are added in quadrature for each image.

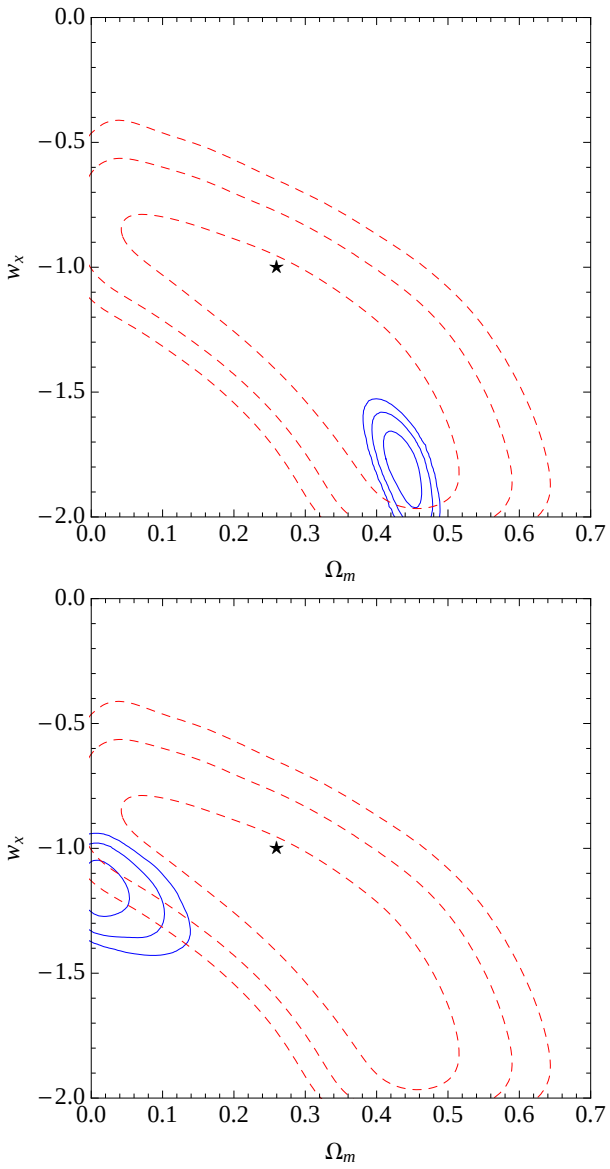

Figure 8. The effect of underestimating errors in CSL for a single cluster. Top panel: the solid contours assume astrometric uncertainties of only 0.1 arcseconds on the image positions, neglecting all sources of modeling error. The dashed contours correspond to parameter recovery using the full error estimate, accounting for perturbations due to scatter in the cluster galaxy population, LOS halos, and astrometric errors. The input model is depicted by a star. Underestimating the total error can lead to erroneous constraints on the dark energy equation-of-state. Bottom panel: the solid contours show the effect of using photometric redshifts for the high-redshift half of the image catalog. For these images, photometric redshift errors are simulated by drawing redshifts from a Gaussian distribution with standard deviation of 0.5. The full error estimates are used for all images. The dashed contours are the same as in the top panel.

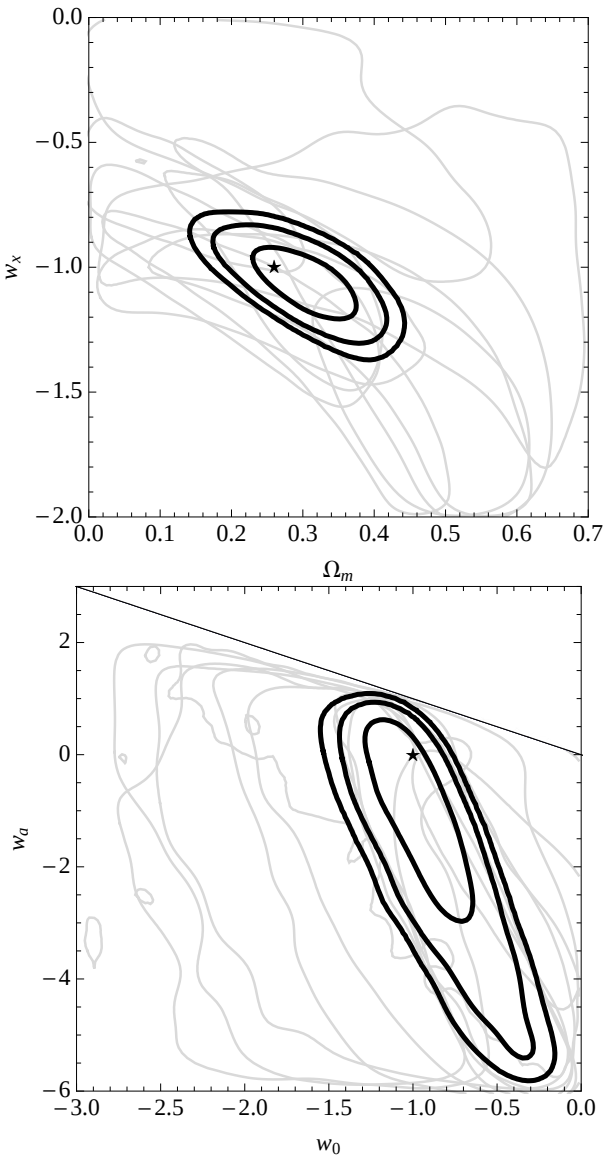

Figure 9. Simulated CSL constraints on the dark energy equation-of-state derived from 10 clusters with 20 multiply-imaged families each. The dark contours show the 68, 95, and 99 per cent confidence regions in the ensemble result. The light contours correspond to the 1-σ regions from individual clusters. The stars correspond to the input model (ΛCDM). The simulated image catalogs include perturbations due to scatter in the cluster galaxy populations, line-of-sight halos, and observational errors on the image positions and redshifts. Top panel: marginalized PDF in the w_x and Ω_m plane. Bottom panel: simulated constraints on the CPL parameterization for the same ten clusters as the top panel in the $w_a - w_0$ plane. The line shows the border of the $w_a < -w_0$ prior. We note that despite the inability to reproduce observed image positions to within ~ 1 arcsecond (see Table 2), useful constraints can be obtained by combining results from independent clusters.

Note that we have used the fiducial input models for each cluster to estimate errors. In practice, one does not have a priori information about the smooth cluster component, cluster-galaxy scaling relations, or source positions. This information would be required to perform the above Monte Carlo simulations. An initial fit using the image positions would therefore be necessary as a starting point for the Monte Carlo simulations in this work. Using the initial fit, one could then transform the observed images to the source plane. Since the initial mass model would not be a perfect fit, images from the same source would not necessarily trace back to the same source position. One way around this problem is to take the barycenters of positions corresponding to single sources. The set of barycenters would constitute a model source catalog to base the Monte Carlo simulations on. For more details on how Monte Carlo based error estimation would be performed in practice, we refer the reader to a recent paper on the cluster Abell 1689 that we have co-authored: Jullo et al. (2010).

We first illustrate the importance of correctly estimating uncertainties. Figure 8 shows the contours of the marginalized PDF obtained from a single cluster using a mock image catalog of 20 families which has been perturbed by scatter in the cluster galaxies, LOS halos, and observational errors. From here on, the outer, middle and inner contours of PDFs correspond to 99, 95, and 68 per cent levels respectively. We utilize the simple model described in Section 3, whose parameters are listed in Table 1 to perform the parameter recovery. The dashed contours show the confidence regions obtained using the full error estimates, which account for all perturbations to image locations in our simulations. The solid contours in the top panel underestimate the uncertainties by assuming only observational errors of 0.1 arcsecond. Note that this is an order of magnitude smaller than typical perturbations obtained in Section 4. The input model, denoted by a star, is definitively ruled out when the errors are underestimated. The bottom panel of Figure 8 shows the effect of using photometric redshifts. We simulate errors for the high-redshift half of the image catalog by redrawing from Gaussian distributions with standard deviations of 0.5. The full positional errors are used for both sets of contours in the bottom panel. Spectroscopically measured redshifts are necessary to minimize the effect of observational uncertainties in CSL cosmography.

Figure 9 shows the results of combining constraints from our simulated ten-cluster sample, where all errors have been fully accounted for. The top and bottom panels correspond to the constant equation-of-state and CPL parameterizations respectively. We checked the stability of the results by running the MCMC ten times for each cluster. Table 2 shows the properties of each cluster in the sample. The image plane root-mean-square (RMS) deviations are frequently used in strong lensing studies to quantify how well a particular model reproduces the observed images. For a given family with n images it is defined to be

$$\mathrm{RMS} = \sqrt{\frac{1}{n}\sum_{i=1}^{n}\left(\vec{\theta}_o^{\,i} - \vec{\theta}^{\,i}\right)^2} \tag{11}$$

where $\vec{\theta}_o^{\,i}$ is the observed image position and $\vec{\theta}^{\,i}$ is the model image position. The total RMS for a given model is obtained by averaging (11) over all observed families. The last column of Table 2 shows that, for a given cluster, the parametric models are not able to reproduce image configurations to within ~ 1 arcsecond. In fact, we should not expect them to perform any better due to the errors discussed in Section 4. However, Figure 9 indicates that the effect of these errors can be alleviated by using a relatively small sample of clusters. Dark energy constraints from CSL can therefore start to be competitive with constraints from other cosmological techniques upon combining just ~ 10 clusters with ~ 20 families each.

Table 2. Properties of simulated clusters.

Redshift	Mass[a] ($\times 10^{15}$ $M_\odot$)	Mass in core galaxies ($\times 10^{13}$ $M_\odot$)	Image plane RMS[b] (arcseconds)
0.208	1.19	7.4	1.01
0.336	1.27	4.8	0.74
0.184	1.11	4.6	0.76
0.246	1.41	4.3	1.02
0.241	1.37	1.4	0.71
0.278	1.38	3.2	0.52
0.284	1.16	3.3	0.98
0.226	1.34	6.1	0.49
0.204	1.39	4.0	0.70
0.244	1.39	7.0	1.30

[a] The total mass within a circular aperture of 1 Mpc.
[b] Averaged over all MCMC samples. Here, we quote the results for the constant w_x case.

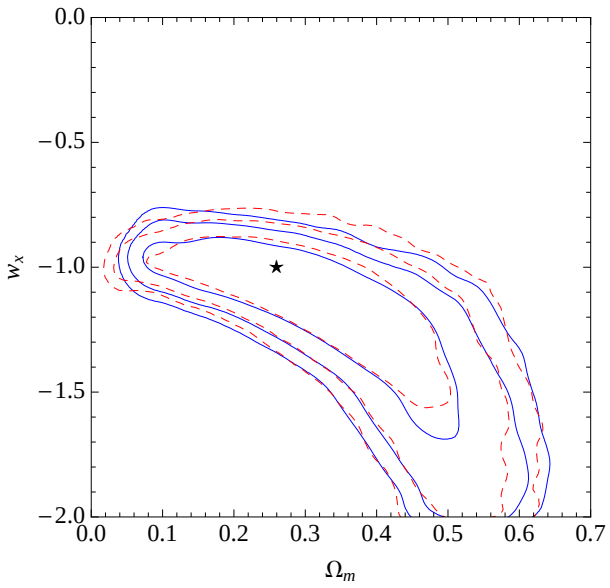

Figure 10. Simulated dark energy constraints obtained from two cluster lenses with the same total mass modeled using two different mass profiles. The solid and dashed contours correspond to PIEMD and NFW lenses respectively. For both cases we use mock catalogs of 21 images. We assume only observational errors of 0.1 arcseconds for each image. The similarity of the results illustrates that CSL cosmography is not contingent upon choice of mass profiles, but may in principle be applied to any strong lensing system with sufficient constraints.

6 CLUSTER MASS PROFILES

The main goal of this section is to show that CSL cosmography is not limited by the choice of mass profiles used to model clusters. As pointed out in Section 2, the CSL technique is a geometric probe that exploits the dependence of lensed image locations on angular diameter distances. In principle, it can be applied to any strong lensing system, irrespective of the mass distribution of the lens, as long as a sufficient number of constraints are observed to accurately model the system.

Although we have used PIEMD lenses exclusively in this work, our results are not contingent upon this choice of profile. To illustrate this point, we use the Navarro-Frenk-White profile, which has a cusp with the density approaching r^{-1} in the inner regions, and transits to r^{-3} in the outer regions beyond the scale radius (Navarro et al. 1995, 1996, 1997). This profile is significantly different from the PIEMD case. For lensing properties of the NFW profile and an elliptical extension of it, we refer the reader to Bartelmann (1996) and Golse & Kneib (2002) respectively.

For comparison, we generate elliptical PIEMD and NFW lenses at a redshift of $z_l = 0.21$ with equal masses of 1.6×10^{15} $M_\odot$. The former has a velocity dispersion of 1300 km/s, core radius of 41 kpc and scale radius of 900 kpc. The latter has a concentration parameter $c = 4.5$ and a scale radius $r_s = 495\,\mathrm{kpc}$. Both have ellipticity parameters of 0.3. Since our purpose in this section is solely to compare different cluster-scale mass profiles, we neglect the role of sub-structure in what follows. We lens a simulated source distribution for both cases and use the same number of images as constraints for parameter recovery. We run the MCMC sampler using the input models with flat priors. In the NFW case all parameters are free. In the PIEMD case, we fix $r_{\rm core}$ to the input value so that the number of free parameters is the same in the two cases. Figure 10 compares the results from both cases. The solid and dashed contours show the PIEMD and NFW constraints respectively. We note the similarity of the results, indicating that a sample of NFW cluster lenses would generally yield similar constraints to those shown in Section 5.

In this work we have utilized unimodal lenses consisting of only one large-scale halo and a population of galaxy-scale subhalos to model the mass distribution. In reality, cluster lenses can be more complex than this, requiring a multi-modal mass distribution to fit the observed images. Here, we address the question of whether bimodal clusters (for example, Abell 1689; Abell 2218; Cl0024+16) can be useful for CSL cosmography.

We use the simulated PIEMD cluster above as a unimodal reference. We simulate bimodal lenses with mass equally divided between the two mass peaks and total masses equal to the reference lens. We generate 10 different lensing configurations for the bimodal case using 10 unique source catalogs and random orientations of the two mass peaks. We then recover the cosmological parameters for each realization using the same number of images as the reference configuration. Results from the bimodal realization with the widest constraints are shown as the dashed contours in Figure 11. The solid contours correspond to the unimodal reference lens. Surprisingly, despite the increase in the number of free parameters, the bimodal constraints are generally similar to the unimodal constraints. This result is robust for various bimodal configurations and for various ratios of the two mass peaks. The tightness of the bimodal constraints is likely due to both the higher amplification of images, on average, and to degeneracies between parameters which limit the number of effective free parameters. We conclude that despite the larger number of parameters required to model bimodal cluster lenses, these systems may be just as useful for CSL cosmography as their unimodal counterparts. Note, however, that we have considered a highly idealized model and have not taken

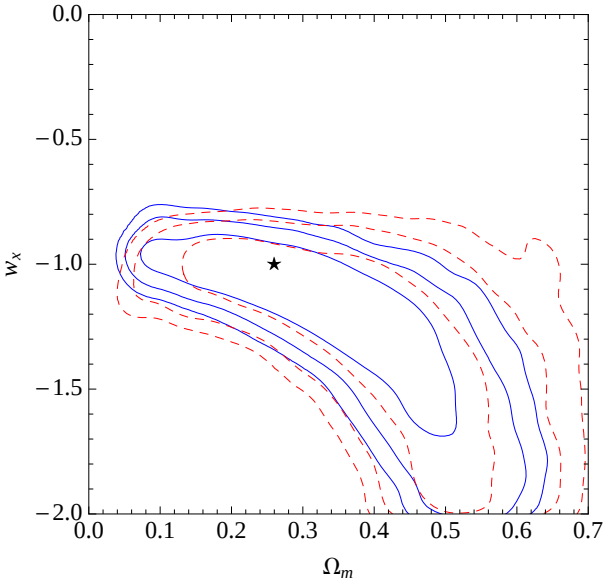

Figure 11. Same as in Figure 10, except that the dashed contours correspond to a bimodal cluster consisting of two PIEMD mass peaks. Despite having twice the number of free parameters, the bimodal constraints are very similar to the unimodal case.

into account the increased modeling errors that would likely result from more complex mass distributions. In addition to the difficulty in modeling more complicated systems, the increased errors would act to weaken the dark energy constraints and possibly introduce biases. We defer a more detailed analysis of more realistic cluster mass distributions derived from high resolution cosmological N-body simulations to future work.

7 DISCUSSION

We have shown that, using a relatively small ($\sim$ 10 galaxy clusters) sample of well constrained cluster lenses with parametric mass models, it may be possible to obtain constraints on the dark energy equation of state and its time variation that are competitive with existing probes. Cluster strong lensing may provide a very useful complementary tool, particularly in probing dynamic dark energy models, which are currently poorly constrained, in the near future.

We have used simple Monte-Carlo simulations of cluster lensing configurations to explore some of the potentially largest sources of modeling errors. Owing to the large number of parameters that would be required to accurately model the cluster galaxy population, parametric models must assume scaling relations between galaxy luminosities and their mass profile parameters. While these assumptions generally improve agreement with observed images, we have shown that scatter in the scaling relations can introduce modeling errors as large as $\sim$ 1 arcsecond for clusters at $z \sim 0.2 - 0.3$.

We have used publicly available halo catalogs from the Millennium Simulation in order to quantify the lensing effects of intervening halos along the line-of-sight between the observer and the background sources. Owing to limited observational resources at the present, most of these halos would not be modeled in practice, and could potentially add significantly to the CSL error budget. A redshift survey behind the most massive lensing clusters would be required to explicitly include structures along the line of sight in the modeling. We created an ensemble of line-of-sight realizations containing analytic galaxy-scale potentials. Using a multi-plane lensing algorithm, we traced light rays through each line-of-sight realization, with the simulated cluster placed at the appropriate redshift. Although LOS halos typically contribute less than $\sim$ 10 per cent to the efficiency-weighted surface mass densities, they can introduce deflections with respect to cluster-only models that are typically on the order of a few arcseconds for clusters at $z \sim 0.2 - 0.3$. In rare cases, deflections can be as large as $\sim$ 10 arcseconds.

Given the fact that scatter in the cluster galaxy population and LOS halos perturb images typically by a few arc seconds, simple parametric models cannot be expected to reproduce image locations to within this accuracy. We have shown that underestimating the total errors can lead to severe biases in dark energy parameter recovery. This is particularly relevant in the case of space-based imaging and spectroscopically obtained redshifts, where observational errors are typically of the order of $\sim$ 0.1 arcseconds - an order of magnitude lower than potential modeling errors.

We have used our Monte-Carlo simulations to perform a feasibility test on obtaining competitive dark energy constraints from CSL systems. We used a sample of 10 clusters with 20 multiply imaged sources each. These sources have redshifts between $z \sim 0.7 - 5$. The simulated image catalogs take into account deflections due to scatter in the cluster galaxy scaling relations and intervening LOS halos. We also simulated observational errors on positions and redshifts. For each simulated cluster lens, we used a Bayesian MCMC technique to probe the dark energy equation-of-state. We found that the observed images only need to be reproduced to within $\sim$ 1 arcsecond on average to get useful constraints upon combining results from $\sim$ 10 clusters.

Our feasibility test expands on the work of Dalal et al. (2005) in a number of ways. Perhaps most importantly, we have shown that Bayesian Inference with Markov Chain Monte-Carlo can be used to avoid biases that may occur in a best-fit approach by probing the full range of parameters that are statistically compatible with the image data. Crucial to this point is the use of accurate error estimates on image positions, obtained by a detailed analysis of each individual cluster, and models containing sufficient degrees of freedom to incorporate complexities such as substructure. The large range of cosmological parameters compatible with a single lensing system can be narrowed by combining results from different systems.

While our simulations have allowed us to explore some of the main difficulties in CSL cosmography in a straightforward way, there are some important limitations which we plan to address in future work. First, our calculation on the effects of the line-of-sight includes only mass in collapsed halos within the field of view. In reality, the light rays are influenced by an extended network of larger scale structures. The mass exterior to halos also contributes significantly to the overall deflection of light rays. However, for our purposes, the relevant quantities are the relative deflections between the observed images, which are typically separated by tens of arcseconds. We plan to explore the impact of extended large-scale structure in future work exploiting the full particle data and periodic boundary conditions of a high resolution cosmological N-body simulation.

Another key limitation is that we have used the same parametric profile for the smooth, large-scale component of both the input and recovery models. While our focus in this work was primarily on the influence of substructure and line-of-sight halos, it will be important in future work to test the influence of uncertainties in the large-scale component. In Figure 2 of their paper, Dalal et al.

(2005) show that using a parametric profile different from the input model can lead to significant biases in the parameter recovery. We have performed our own tests attempting to recover PIEMD lenses with NFW models and vice versa. We found that the Bayesian sampler did not converge and that the poorness of fit was reflected in the evidence values. In practice, it should be straightforward to determine if the model for the large-scale component generally fails to reflect the true mass distribution (i.e. utilizing RMS deviations between model and observed images and comparison of Bayesian evidence values). However, uncertainties due to less obvious deviations in the large-scale component is a topic that needs to be explored.

In upcoming work, it will also be crucial to test how well parametric models can be used to describe more complex cluster mass distributions. In principal, more sophisticated models can be introduced for these systems (e.g. Diego et al. 2005a,b; Coe et al. 2008; Jullo & Kneib 2009; Coe et al. 2010). With $\sim$ 20 families, there are certainly enough constraints to increase the number of free parameters. However, doing so may degrade the efficacy of derived cosmological constraints and introduce additional modeling errors and degeneracies. It may be possible to alleviate this problem by simply obtaining a larger sample of cluster lenses or including additional independent constraints. Note that we have investigated the use of strongly lensed image positions and redshifts, but have not considered other possible sources of information. Inclusion of X-ray gas temperature profiles, measured cluster velocity dispersions, and the stellar velocity dispersion profiles of bright cluster galaxies may enable the tightening of derived cosmological constraints with more sophisticated mass models.

We conclude with a brief discussion on observational strategy. Clearly, the ideal cluster lensing system for cosmography would have a relatively simple mass distribution with a large number of observed images. However, in practice, there will likely be a trade-off between complex lensing systems that produce a larger number of strongly lensed images and simple systems with fewer constraints. This is due to the possible enhancement of strong lensing cross sections from substructure and asymmetries (e.g. Bartelmann et al. 1995; Meneghetti et al. 2007), mergers (e.g. Torri et al. 2004; Fedeli et al. 2006) and line-of-sight matter (e.g. Wambsganss et al. 2005; Hennawi et al. 2007; Hilbert et al. 2007; Puchwein & Hilbert 2009). The most dramatic and readily observable cluster strong lenses are likely to be more complicated to model. However, in section 6 we showed that a larger number of model parameters does not necessarily correspond to weaker dark energy constraints. Therefore, it may not be wise to devote all resources towards the simplest lensing systems with the fewest sources of uncertainty. The complex systems are probably easier to find and may provide equal or more leverage on cosmological parameters. These benefits may outweigh the costs of more detailed analyses. Complex and simple cluster lensing systems are likely to play complementary roles in cosmographic applications.

ACKNOWLEDGMENTS

The authors thank Eric Jullo and Jean-Paul Kneib for insightful discussions and the anonymous referee for helpful comments and suggestions. PN acknowledges the receipt of a Guggenheim Fellowship from the John P. Simon Guggenheim Foundation, a Radcliffe Fellowship from the Radcliffe Institute for Advanced Study, and a grant from the National Science Foundation's Theory Program (AST10-44455).

REFERENCES

Allen S. W., Schmidt R. W., Ebeling H., Fabian A. C., van Speybroeck L., 2004, MNRAS, 353, 457
Bacon D. J., Refregier A. R., Ellis R. S., 2000, MNRAS, 318, 625
Barnabè M., Czoske O., Koopmans L. V. E., Treu T., Bolton A. S., Gavazzi R., 2009, MNRAS, 399, 21
Bartelmann M., Steinmetz M., Weiss A., 1995, A&A, 297, 1
Bartelmann M., 1996, A&A, 313, 697
Bolton A. S., Treu T., Koopmans L. V. E., Gavazzi R., Moustakas L. A., Burles S., Schlegel D. J., Wayth R., 2008, ApJ, 684, 248
Broadhurst T., Benítez N., Coe D., et al. 2005, ApJ, 621, 53
Chevallier M., Polarski D., 2001, IJMPD, 10, 213
Coe D., Benitez N., Broadhurst T., Moustakas L., Ford H., 2010, ArXiv e-prints
Coe D., Fuselier E., Benítez N., Broadhurst T., Frye B., Ford H., 2008, ApJ, 681, 814
Cooray A. R., 1999, ApJ, 524, 504
Dalal N., Hennawi J. F., Bode P., 2005, ApJ, 622, 99
D'Aloisio A., Furlanetto S. R., Natarajan P., 2008, MNRAS, 394, 1469
Diego J. M., Protopapas P., Sandvik H. B., Tegmark M., 2005a, MNRAS, 360, 477
Diego J. M., Sandvik H. B., Protopapas P., Tegmark M., Benítez N., Broadhurst T., 2005b, MNRAS, 362, 1247
Ebeling H., Edge A. C., Henry J. P., 2001, ApJ, 553, 668
Efstathiou G., Moody S., Peacock J. A., et al. 2002, MNRAS, 330, L29
Eisenstein D. J., Zehavi I., Hogg D. W., et al. 2005, ApJ, 633, 560
Elíasdóttir Á., Limousin M., Richard J., Hjorth J., Kneib J., Natarajan P., Pedersen K., Jullo E., Paraficz D., 2007, ArXiv e-prints
Fedeli C., Meneghetti M., Bartelmann M., Dolag K., Moscardini L., 2006, A&A, 447, 419
Fernández-Soto A., Lanzetta K. M., Yahil A., 1999, ApJ, 513, 34
Gao L., Navarro J. F., Cole S., Frenk C. S., White S. D. M., Springel V., Jenkins A., Neto A. F., 2008, MNRAS, 387, 536
Gilmore J., Natarajan P., 2009, MNRAS, 396, 354
Golse G., Kneib J., 2002, A&A, 390, 821
Golse G., Kneib J., Soucail G., 2002, A&A, 387, 788
Grossi M., Springel V., 2009, MNRAS, 394, 1559
Halkola A., Seitz S., Pannella M., 2006, MNRAS, 372, 1425
Harsono D., De Propris R., 2009, AJ, 137, 3091
Hennawi J. F., Dalal N., Bode P., Ostriker J. P., 2007, ApJ, 654, 714
Hilbert S., White S. D. M., Hartlap J., Schneider P., 2007, MNRAS, 382, 121
Hilbert S., Hartlap J., White S. D. M., Schneider P., 2009, A&A, 499, 31
Jullo E., Kneib J., 2009, MNRAS, 395, 1319
Jullo E., Kneib J.-P., Limousin M., Elíasdóttir Á., Marshall P. J., Verdugo T., 2007, New Journal of Physics, 9, 447
Jullo E., Natarajan P., Kneib J., D'Aloisio A., Limousin M., Richard J., Schimd C., 2010, Science, 329, 924
Kaiser N., Wilson G., Luppino G. A., 2000, ArXiv Astrophysics e-prints
Kassiola A., Kovner I., 1993, ApJ, 417, 450
Kneib J., Ellis R. S., Smail I., Couch W. J., Sharples R. M., 1996, ApJ, 471, 643
Kneib J., Hudelot P., Ellis R. S., Treu T., Smith G. P., Marshall P., Czoske O., Smail I., Natarajan P., 2003, ApJ, 598, 804
Komatsu E., Smith K. M., Dunkley J., et al. 2010, ArXiv e-prints
Kowalski M., Rubin D., Aldering G., et al. 2008, ApJ, 686, 749
Limousin M., Richard J., Jullo E., Kneib J.-P., Fort B., Soucail G., Elíasdóttir Á., Natarajan P., Ellis R. S., Smail I., Czoske O., Smith G. P., Hudelot P., Bardeau S., Ebeling H., Egami E., Knudsen K. K., 2007, ApJ, 668, 643
Limousin M., Richard J., Kneib J., Brink H., Pelló R., Jullo E., Tu H., Sommer-Larsen J., Egami E., Michałowski M. J., Cabanac R., Stark D. P., 2008, A&A, 489, 23
Linder E. V., 2003, Physical Review Letters, 90, 091301
Link R., Pierce M. J., 1998, ApJ, 502, 63
Macciò A. V., 2005, MNRAS, 361, 1250
Meneghetti M., Bartelmann M., Dolag K., Moscardini L., Perrotta F., Bac-

cigalupi C., Tormen G., 2005b, A&A, 442, 413
Meneghetti M., Jain B., Bartelmann M., Dolag K., 2005a, MNRAS, 362, 1301
Meneghetti M., Argazzi R., Pace F., Moscardini L., Dolag K., Bartelmann M., Li G., Oguri M., 2007, A&A, 461, 25
Natarajan P., Kneib J., Smail I., 2002, ApJ, 580, L11
Natarajan P., Kneib J., Smail I., Ellis R. S., 1998, ApJ, 499, 600
Natarajan P., Kneib J., Smail I., Treu T., Ellis R., Moran S., Limousin M., Czoske O., 2009, ApJ, 693, 970
Navarro J. F., Frenk C. S., White S. D. M., 1995, MNRAS, 275, 56
Navarro J. F., Frenk C. S., White S. D. M., 1996, ApJ, 462, 563
Navarro J. F., Frenk C. S., White S. D. M., 1997, ApJ, 490, 493
Neto A. F., Gao L., Bett P., Cole S., Navarro J. F., Frenk C. S., White S. D. M., Springel V., Jenkins A., 2007, MNRAS, 381, 1450
Paczynski B., Gorski K., 1981, ApJ, 248, L101
Perlmutter S., Aldering G., Goldhaber G., et al. 1999, ApJ, 517, 565
Puchwein E., Hilbert S., 2009, MNRAS, 398, 1298
Richard J., Kneib J., Limousin M., Edge A., Jullo E., 2010a, MNRAS, 402, L44
Richard J., Pei L., Limousin M., Jullo E., Kneib J. P., 2009, A&A, 498, 37
Richard J., Smith G. P., Kneib J., Ellis R. S., Sanderson A. J. R., Pei L., Targett T. A., Sand D. J., Swinbank A. M., Dannerbauer H., Mazzotta P., Limousin M., Egami E., Jullo E., Hamilton-Morris V., Moran S. M., 2010b, MNRAS, 404, 325
Riess A. G., Filippenko A. V., Challis P., et al. 1998, AJ, 116, 1009
Schneider P., Ehlers J., Falco E. E., 1992, Gravitational Lenses
Seljak U., Makarov A., McDonald P., et al. 2005, PRD, 71, 103515
Semboloni E., Mellier Y., van Waerbeke L., Hoekstra H., Tereno I., Benabed K., Gwyn S. D. J., Fu L., Hudson M. J., Maoli R., Parker L. C., 2006, A&A, 452, 51
Sereno M., 2002, A&A, 393, 757
Smith G. P., Ebeling H., Limousin M., Kneib J., Swinbank A. M., Ma C., Jauzac M., Richard J., Jullo E., Sand D. J., Edge A. C., Smail I., 2009, ApJ, 707, L163
Soucail G., Kneib J., Golse G., 2004, A&A, 417, L33
Springel V., White S. D. M., Jenkins A., Frenk C. S., Yoshida N., Gao L., Navarro J., Thacker R., Croton D., Helly J., Peacock J. A., Cole S., Thomas P., Couchman H., Evrard A., Colberg J., Pearce F., 2005, Nature, 435, 629
Torri E., Meneghetti M., Bartelmann M., Moscardini L., Rasia E., Tormen G., 2004, MNRAS, 349, 476
Van Waerbeke L., Mellier Y., Erben T., Cuillandre J. C., Bernardeau F., Maoli R., Bertin E., McCracken H. J., Le Fèvre O., Fort B., Dantel-Fort M., Jain B., Schneider P., 2000, A&A, 358, 30
Vikhlinin A., Kravtsov A. V., Burenin R. A., Ebeling H., Forman W. R., Hornstrup A., Jones C., Murray S. S., Nagai D., Quintana H., Voevodkin A., 2009, ApJ, 692, 1060
Wambsganss J., Bode P., Ostriker J. P., 2005, ApJ, 635, L1
Wittman D. M., Tyson J. A., Kirkman D., Dell'Antonio I., Bernstein G., 2000, Nature, 405, 143
Yahata N., Lanzetta K. M., Chen H., Fernández-Soto A., Pascarelle S. M., Yahil A., Puetter R. C., 2000, ApJ, 538, 493